Journal of Materials Chemistry C

Insights into the Chemistry of Vapor Phase Infiltration for Imaging Non-Fullerene Acceptors

Journal:	*Journal of Materials Chemistry C*
Manuscript ID	TC-ART-04-2022-001643.R1
Article Type:	Paper
Date Submitted by the Author:	24-May-2022
Complete List of Authors:	Nahor , Oded; Technion Israel Institute of Technology, Materials Science and Engineering Cohen, Anthony; Technion Israel Institute of Technology, Schulich Faculty of Chemistry Frey, Gitti; Technion Israel Institute of Technology, Department of Materials Science & Engineering; Technion Israel Institute of Technology,

Insights into the Chemistry of Vapor Phase Infiltration for Imaging Non-Fullerene Acceptors

Oded Nahor [a], Anthony Cohen [b], and Gitti L. Frey [a,*]

[a] Department of Material Science and Engineering, Technion - Israel Institute of Technology, Haifa 3200003, Israel

[b] Schulich Faculty of Chemistry, Technion - Israel Institute of Technology, Haifa 3200003, Israel

*gitti@technion.ac.il

Abstract

Vapor phase infiltration (VPI) processes offer a unique method to form hybrid materials by growing inorganic species inside polymer matrices from gaseous precursors. The VPI process follows three main stages: sorption of the gas phase precursors to the polymer matrix, their diffusion and entrapment in the matrix, and the chemical reaction. The distinct entrapment character of the precursors in different matrices can be utilized for imaging organic blends by selectively "staining" one component of the blend and imaging a cross-section in electron microscopy. Organic solar cell (OSC) films are an excellent platform to study VPI "staining" because they are composed of organic blends, a polymeric electron donor, and a small molecule electron acceptor (SMA), in a bulk heterojunction (BHJ) morphology. Currently, OSCs based on non-fullerene acceptors (NFA) exhibit high efficiencies making them the focal point and most promising for future technology development. Yet, the phase behavior and intricate details of the film morphologies are not fully understood. In this study we develop a method for direct imaging of NFA-based OSC blend morphology. We focus on the most investigated NFA, 3,9-bis(2-methylene-(3-(1,1-dicyanomethylene)-indanone))-5,5,11,11-tetrakis(4-hexylphenyl)-dithieno[2,3-d:2',3'-d']-s-indaceno[1,2-b:5,6-b']dithiophene(ITIC) and apply different diethylzinc VPI protocols and reveal a strong chemical

reaction between diethylzinc (DEZ), the gaseous precursor, and ITIC. This reaction leads to a unique staining mechanism with distinct feature characteristics. A similar reaction is also demonstrated for other NFAs that are currently popular in high-efficiency OSCs, confirming the suitability of this new methodology for imaging OSCs. These results give insights not only for imaging OSCs but also for developing VPI-based staining and imaging of other functional organic blends.

Introduction

Exposing polymeric substrates to traditional atomic layer deposition (ALD) can result in the diffusion of the gas phase molecular precursors into the polymer matrix, followed by their sub-surface deposition to form hybrid organic-inorganic materials. Several approaches for "sub-surface ALD" were developed, including sequential infiltration synthesis (SIS)[1], multiple pulse infiltration (MPI)[2], sequential vapor infiltration (SVI)[3], etc. Although the terminology is different, they all share similar atomic-scale mechanisms and are hence unified under the vapor phase infiltration (VPI) ambarella[4]. The VPI process consists of two consecutive stages. First, an organometallic gas is pulsed into the sample chamber followed by a purge process, then a second pulse of a complementary precursor, most commonly water, is introduced and purged. The number of cycles, pulse pressure, purge time, temperature, and most importantly, the type of polymer matrix and molecular precursors, determine the composition and structure of the obtained hybrid material. The mechanistic principles were extensively studied in recent years and recently reviewed by Leng et al.[4] and Waldman et al.[5], and can generally be described by three consecutive processes: sorption, diffusion, and entrapment of the precursors in the organic matrix.

The extent of precursor entrapment in the polymer matrix depends on process conditions such as pressure and temperature and on the interaction between the matrix material and the precursor molecules. More specifically, physical entrapment occurs when the polymer matrix is non-reactive so that the precursors diffuse into the polymer and randomly nucleate and grow inorganic particles inside. The particles are simply embedded in the free volume of the matrix with weak or no interaction with the host[6]. Chemical entrapment, on the other hand, occurs when the host matrix has functional moieties, such as Lewis bases, that can react with the precursors leading to the retainment of the precursor chemically bound to specific functional groups. Under such conditions, the inorganic particles nucleate and grow from those functional moiety sites. One of the most familiar examples of a reactive polymer/precursor couple is the poly(methyl methacrylate)/trimethylaluminum (PMMA/TMA) pair[7–14]. It was shown that at temperatures above 100 °C, the carbonyl moiety of PMMA reacts with TMA leading to a covalent bond followed by nucleation and growth of Al_2O_3 particles[9]. However, below 100 °C, a metastable complex in the form of a reversible

coordination bond is formed between PMMA and TMA. Under such conditions, the retainment of TMA in the PMMA matrix has more physical than chemical character.

VPI was utilized for various applications such as enhancing mechanical and chemical properties of polymeric fibers[15], improving chemical resistance[16], the design and synthesis of bio-inspired materials[17], and block co-polymer-templated inorganic nanostructures towards patterning[18]. Recently, VPI was suggested as a method to selectively introduce a contrasting agent into multi-phase all-organic functional thin films for imaging by electron microscopy[19]. Since the organic compounds share similar building elements with similar atomic numbers (carbon, oxygen, nitrogen, etc.), it is extremely difficult to distinguish between different components and/or different phases in a generally amorphous blend film using electron microscopy techniques. Furthermore, organic films are generally susceptible to electron beam damage during the analysis. Therefore, the deposition of inorganic particles in selective domains in the film can be used as both contrast agents, similar to the staining process used for imaging biological specimens for electron microscopy, and film stabilization under the electron beam[6]. For example, exposing a thin film of poly(3-hexylthiophene)/poly(ethylene oxide) (P3HT/PEO) block copolymer to a VPI process of diethyl zinc (DEZ) and water leads to the selective deposition of zinc oxide (ZnO) in PEO domains, as confirmed by electron energy loss spectroscopy (EELS). The analysis showed that the EELS signals of the zinc and sulfur atoms are mutually exclusive, suggesting the favorable association of the ZnO precursors with PEO domains[20]. Therefore, we recently suggested that selective association of the VPI precursors with a component or phase in an organic blend can be used to map the complex morphologies of organic blends, specifically organic solar cell (OSC) films[21].

OSCs are generally composed of two components, a polymeric electron donor and a small molecule acceptor (SMA), usually exhibiting three phases: donor-rich, acceptor-rich, and an intermixed amorphous phase. The desired film morphology is the bulk heterojunction (BHJ) morphology with a 3D interpenetrating network of donor-rich/acceptor-rich domains with the intermixed phase suspended between them. The ideal BHJ should exhibit domain sizes of about 20 nm for maximal optoelectronic performance[22]. For decades, fullerene-based OSC films were investigated and the BHJ morphologies were estimated by various technique[23]; however, direct imaging of the BHJ morphology was scarce[24]. Recently, we harnessed the VPI of DEZ and water for direct imaging of several fullerene-based OSCs blends[21,25,26]. Exposing

the BHJs to VPI leads to ZnO deposition in the free volume of the polymer-rich domains, while the fullerene domains are too dense to allow in-situ ZnO deposition. The selective staining and film stabilization allowed us to perform 3D tomography using a transmission electron microscope, and provide, for the first time, 3D imaging of the complex morphology of a viable fullerene-based OSC films[25].

The introduction of non-fullerene acceptors (NFA) in 2015 led to a significant increase in OSC efficiencies[27,28]. The NFAs are generally constructed of a donor central unit with two acceptor end-capping units, forming an acceptor-donor-acceptor (ADA) molecule[29]. The basic operational principles of NFA-based OSCs are similar to those realized for fullerene-based OSCs, yet the phase behavior and intricate details of NFA-based BHJ morphologies are not fully understood. Therefore, the successful selective staining by VPI of the NFA-based BHJs would significantly contribute to the understanding of their structure-property relationship[28,29].

In this study, we examine the effect of VPI on ADA NFA films to explore the possibility of direct imaging of NFA-based OSC blends. We focus on the most investigated ADA NFA 3,9-bis(2-methylene-(3-(1,1-dicyanomethylene)-indanone))-5,5,11,11-tetrakis(4-hexylphenyl)-dithieno[2,3-d:2',3'-d']-s-indaceno[1,2-b:5,6-b']dithiophene (ITIC), Figure 1a, and apply different DEZ and water VPI protocols. We use UV-vis absorption, FTIR, and NMR to understand the chemical interaction behind the VPI precursors and ITIC and use cross-section high-resolution scanning electron microscopy (HRSEM) imaging to follow the entrapment of the precursors and staining of ITIC films. We find that ITIC is highly reactive to DEZ, and hence, in contrast to the fullerene-based OSC, where staining is due to physical entrapment of the precursors in polymer free-volume, imaging ITIC-based BHJs can be performed by chemical entrapment of the precursors in the NFA domains. The different staining mechanisms also lead to noticeably different feature characteristics so that both polymer and NFA domains can be imaged concurrently, as we demonstrate for P3HT:ITIC bilayers and blends. We also show that similar to ITIC, 2,2'-[[12,13-Bis(2-ethylhexyl)-12,13-dihydro-3,9-diundecylbisthieno[2'',3'':4',5']thieno[2',3':4,5]pyrrolo[3,2-e:2',3'-g][2,1,3]benzothiadiazole-2,10-diyl]bis[methylidyne(5,6-difluoro-3-oxo-1H-indene-2,1(3H)-diylidene)]]bis[propanedinitrile] (Y6), the currently popular ADA NFA, reacts with DEZ which paves the way to utilize this methodology for other high efficiency BHJ OSCs . These results

give insights not only for imaging OSCs but also for developing VPI-based staining and imaging of other functional organic blends.

Results and discussion

First indication of a chemical interaction between ITIC and DEZ, the ZnO VPI precursor, was detected in UV-vis absorption measurements. Annealed thin films of ITIC were exposed to a VPI process of 80 consecutive DEZ pulses followed by a single water pulse at 100 °C (more details on film preparation and VPI process are given in the experimental section). The UV-vis absorption spectra of the ITIC films before (blue line) and after (orange line) the VPI process, Figure 1b, show significant changes to ITIC after the VPI process. The spectrum of the pristine ITIC film exhibits the familiar peak at 704 nm and a shoulder at ~645 nm[27]. These features are completely lost after the VPI process, and new bands rise at 399 and 420 nm. Consequently, the film changed its colors from royal blue before the VPI to pale yellow after the VPI (Figure S1). A similar change in color was previously observed after a chemical reaction between ethanolamine (EA) and ITIC in solution[30]. It was suggested that EA attacks the β-carbon of ITIC, effectively reducing conjugation length and hence a significant blue shift of the absorption. To test the hypothesis of a chemical reaction between ITIC and DEZ, we added a solution of DEZ in toluene[31] to ITIC dissolved in chlorobenzene (CB). The blue color of the ITIC solution changed to orange upon DEZ addition, confirming a chemical reaction. The reaction product was then dried, dissolved in chloroform, and examined by silica thin-layer chromatography (TLC) against an ITIC chloroform solution (Figure S2). The TLC result indicates that ITIC reacted with DEZ to yield a product that is more polar than ITIC.

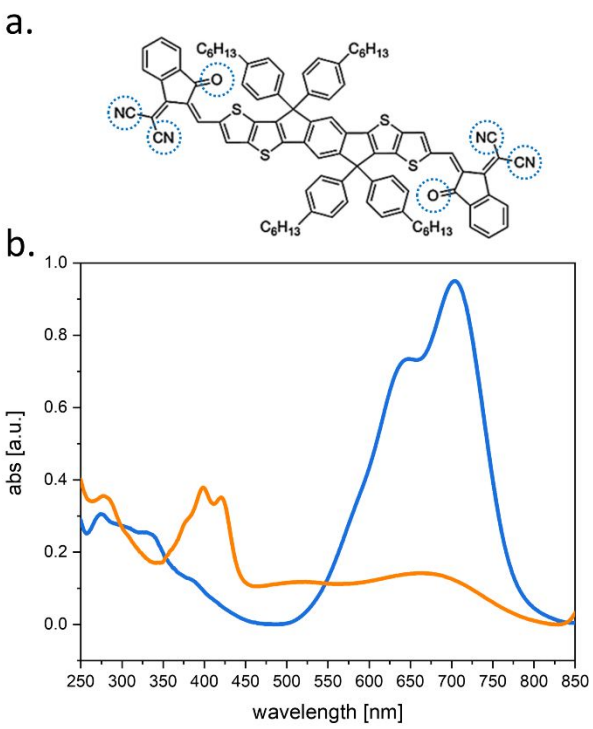

Figure 1- a. Chemical structure of ITIC highlighting the nitrile and carbonyl moieties in blue circles. b. UV-vis absorption spectra of an ITIC film before (blue) and after (orange) exposure to a VPI process with DEZ and water.

The reaction product was further investigated by FTIR. Figure 2a shows the solid-state FTIR spectra of ITIC (blue line) and the ITIC+DEZ reaction product (orange line). The product spectrum is significantly different from that of ITIC, with less pronounced transitions in the conjugated hydrocarbon fingerprint region (about 1400 to 800 cm^{-1}) and two new broad peaks at about 3400 and 480 cm^{-1}. These peaks correspond to the signatures of water[32] and a Zn-O stretching mode[22], respectively, confirming a chemical reaction of ITIC and the formation of a Zn-O moiety. To identify the reaction, we zoom into the 3150-1650 cm^{-1} range (Figure 2b). The ITIC spectrum shows the aliphatic chain bands in the 3000 to 2800 cm^{-1} region and the nitrile (C≡N) and carbonyl (C=O) bands of the end-capped functional moieties at 2218 and 1703cm^{-1}, respectively[32–34]. After the VPI process, the aliphatic bands are maintained, but the nitrile and carbonyl bands change dramatically. More specifically, the carbonyl peak is shifted to a higher wavenumber, 1730cm^{-1}, indicating an increase in bond strength. A similar carbonyl shift was previously reported by Park et al. and assigned to an ITIC vinyl reaction that saturates the carbonyl[34]. The nitrile peak splits to a higher and lower wavenumber doublet at 2227 and 2191 cm^{-1} suggesting two populations with different chemical environments and/or the formation of a coordination bond, similar to an isonitrile, between zinc and nitrogen[33].

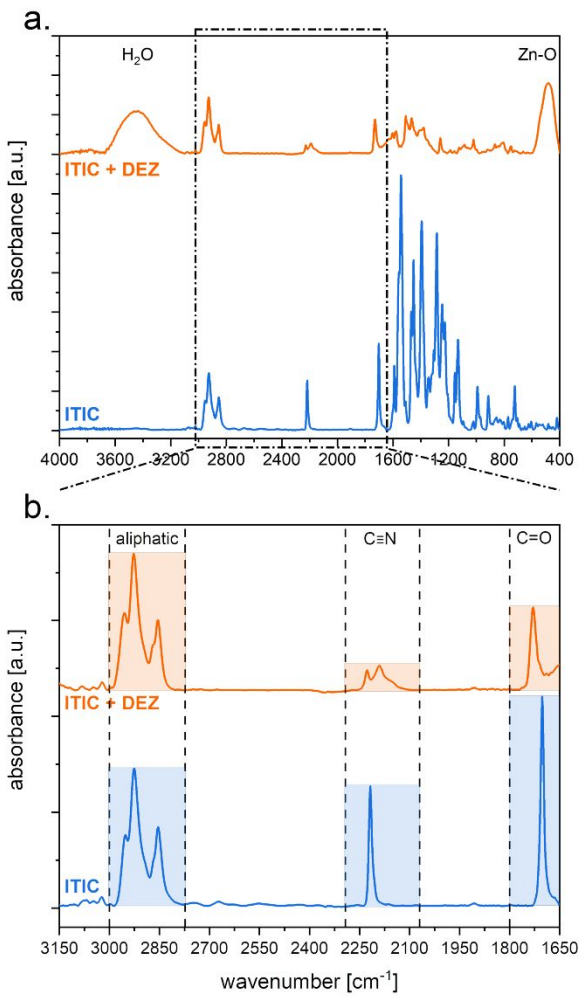

Figure 2- FTIR absorbance spectra of ITIC (blue) and ITIC after a reaction with DEZ (orange): (a) the full wavenumber spectrum recorded, and (b) a zoom-in focusing on the aliphatic (~2900 cm^{-1}), nitrile (~2200 cm^{-1}) and carbonyl (~1700 cm^{-1}) bands. The spectra are normalized to nitrile moiety integration.

Based on the UV-vis and FTIR results we speculate that DEZ reacts with the nitrile groups of ITIC through an extended Michael addition[30], as schematically shown in Scheme 1. In the first stage of this reaction, a reversible coordination bond between DEZ and the nitrile moiety is formed (Scheme S1a.). This brings the ethyl group of DEZ in proximity of the activated double bond next to the thiophene ring. The ethyl nucleophile is then added in a 1,6-conjugate addition, with respect to the malononitrile moiety. This addition results in the formation of a negatively charged nitrogen atom (Scheme S1b.) and increases the binding strength of the molecule to the zinc atom. As a result, the conjugation between the central donor and an end-group acceptor is broken, leading to an increase in the acceptor's carbonyl bond strength, a change in the local chemical environment of one of the nitrile groups, and a significant blue shift in the absorption spectrum. In the case of the VPI process, water is then added to the chamber, and the suggested mechanism of the reaction of water vapor with the

DEZ-reacted ITIC is presented in Scheme S2. The Zn-OH bond that is formed is the nucleus for further growth of ZnO in sequential VPI cycles. For further investigation of the ITIC and DEZ reaction product, we performed full hydrolysis in the solution reaction (Scheme S3), and the adduct was characterized by ^{1}H ,2D COSEY, and ^{13}C NMR spectra, and mass spectroscopy (MS) (Figure S4, Figure S5, Figure S6, and Figure S7, respectively). The results confirm that the reaction between DEZ and ITIC follows the suggested mechanism (see detailed spectra analysis in the Supplementary Information section).

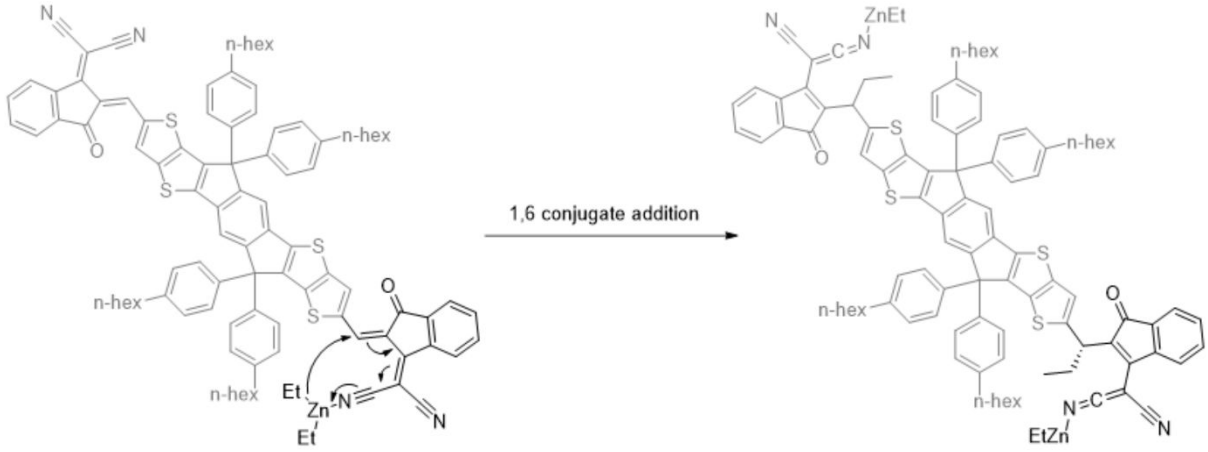

Scheme 1- Suggested mechanism for the reaction between ITIC and DEZ

Finally, we demonstrate the use of the chemical reaction between ITIC and DEZ during VPI to image organic electronic blends. We first compare the cross-section HRSEM micrographs of P3HT and ITIC films after VPI of DEZ and water. P3HT was chosen because it does not react with DEZ during the VPI process[35]; moreover, it was demonstrated that the staining of P3HT by ZnO is due to physical entrapment[6]. The micrograph of P3HT after the VPI process, Figure 3a, shows bright nanoparticles evenly dispersed in the film, confirming the nucleation of ZnO in the free volume of the film, followed by their growth into coarse particles. In contrast, the HRSEM micrograph of the ITIC (Figure 3d) shows a very fine bright contrast throughout the film. This grainy contrast is due to the nucleation of ZnO on numerous ITIC nitrile moieties, leading to evenly spread very fine ZnO clusters. Schematic illustrations of P3HT's physical staining and ITIC's chemical staining are presented in Figures 3b and c, and Figures 3e and f, respectively.

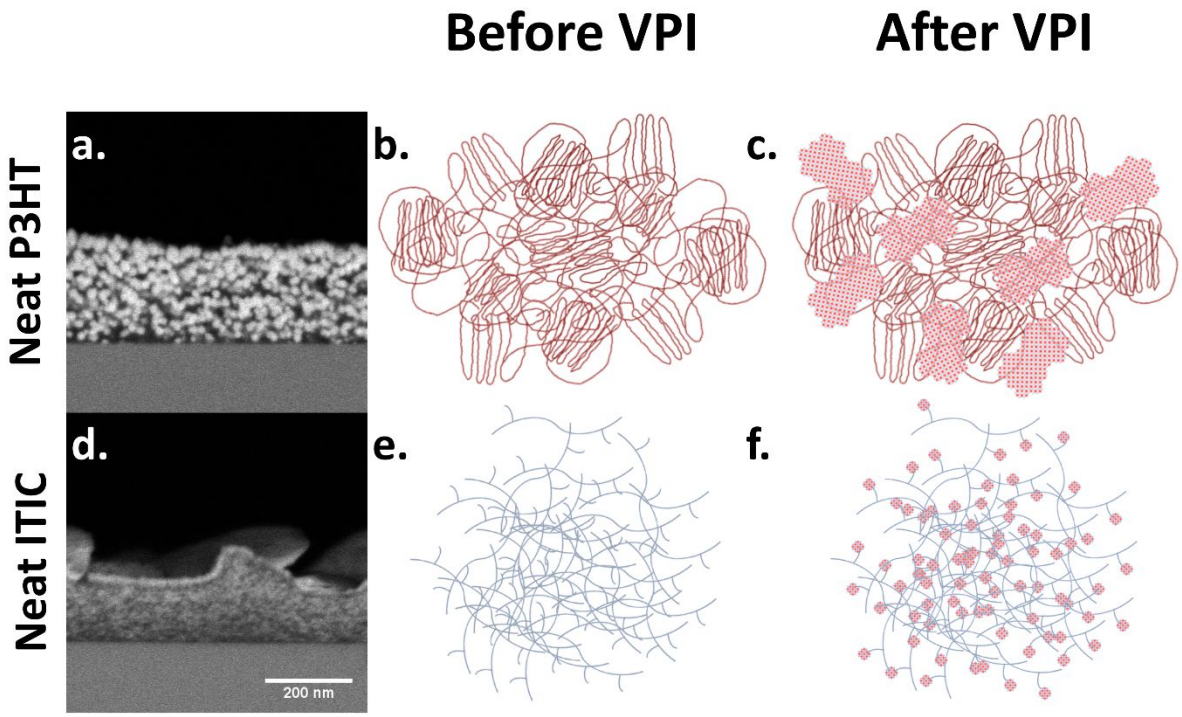

Figure 3- Cross-section HRSEM BSE micrographs and schematic illustrations of P3HT (top) and ITIC (bottom) films before (b,e) and after (a,c and d,f) exposure to the VPI process (100 °C/20 sccm). The P3HT micrograph in a. shows ZnO nanoparticles (bight contrast) evenly distributed in the film. The schematic illustration in b. shows that a pristine P3HT film has crystalline and amorphous domains, and the VPI process results in the deposition of ZnO particles in the amorphous domains of P3H, as shown in c.. In the case of ITIC, micrograph d. shows fine-textured ZnO "mist" (bright) throughout the film. The schematic illustration in e. shows that a pristine ITIC film is generally amorphous, and the VPI process results in the nucleation of ZnO clusters on the ITIC end groups, as shown in f.

We then harnessed the two staining mechanisms to image P3HT:ITIC bilayers. Interestingly, the degree of contrast between the two layers can be tuned by the VPI conditions, specifically the temperature and flow rate. The chemical interaction between DEZ and ITIC leads to the preferable chemical entrapment of the precursor in the bottom ITIC layer. Therefore, under non-diffusion-limited conditions, such as those used here (see experimental section), the typical grainy ZnO staining of the bottom ITIC layer is similar to all VPI processes (Figure 4). For the P3HT top layer; however, increasing temperature from 60 °C to 100 °C depletes the layer from the typical ZnO nanoparticles leaving the P3HT contrast dark (Figures 4a and b) while increasing flow rate (at 100 °C) replenishes their presence in the layer (Figures 4b and c). We suggest that at high temperatures there is sufficient diffusion of the precursor residues out of the P3HT and hence no ZnO deposition. In contrast, a high flow rate increases the chamber pressure causes higher precursor sorption into the polymer and stalls the complete precursor diffusion out of the film. Therefore, these results demonstrate and

provide guidelines for VPI protocols that can be used for selective chemical and physical staining of materials by VPI.

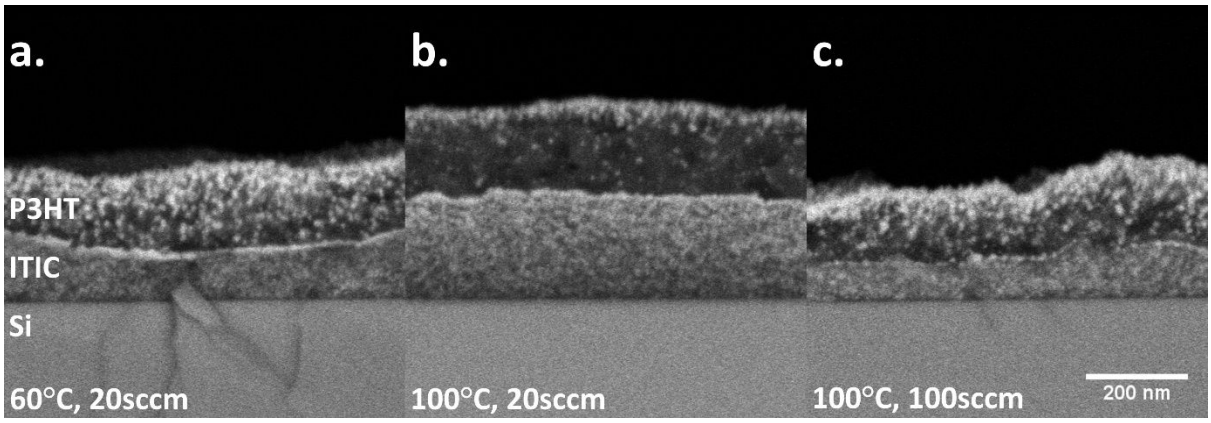

Figure 4- Cross-section HRSEM BSE micrographs of P3HT (top):ITIC (bottom) bilayer films after VPI process of DEZ and water processes at different temperatures and flow rates: (a) 60 °C/20 sccm, (b) 100 °C/20 sccm, and (c) 100 °C/100 sccm. The micrographs show that the VPI conditions strongly affect the character of the ZnO deposited in the P3HT layers ("physical staining") but not that of the ZnO deposited in the ITIC ("chemical staining").

To demonstrate that the differences between chemical and physical staining can be used to reveal complex morphologies by VPI, we prepared BHJ films of the same polymer:SMA system, and exposed them to different precursors. Exposing neat P3HT tetrakis(dimethylamido)hafnium (TDAHf) and water, the precursors of HfO_2, leads to the diffusion and deposition of HfO_2 inside the P3HT film, similar to that of ZnO in P3HT (compare Figures S8a and 3a). On the other hand, TDAHf and water did not infiltrate the pristine ITIC film, probably due to its density[21]. This is in contrast to the ITIC film exposed to DEZ, which showed the misty chemical staining (compare Figures S8b and Figure 3d). The cross-section micrograph of aP3HT:ITIC blend film exposed to the HfO_2 VPI process, Figures 5a and b, shows large, nearly vertically separated bright and dark domains. Following the micrographs in Figure S8, we associate the bright contrast to HfO_2 particles that nucleate and grow in P3HT-rich domains (physical staining) and the dark contrast to impermeable ITIC-rich domains. Interestingly, the cross-section micrograph of the same blend but exposed to the ZnO VPI process also shows large, nearly vertically separated bright and dark domains, Figures 5c and d.. However, in this case, and following Figure 4b, the bright contrast is due to a chemical reaction between DEZ and ITIC (chemical staining) and, hence, associated with ITIC-rich domains. The P3HT domains, on the other hand, are dark due to the diffusion of the precursor residues out of the P3HT, as shown in Figure 4d. Therefore, in the case of this blend, the

physical and chemical staining are complementary, providing nearly negative images of the same BHJ. The comparison between the physical and chemical stained BHJs reveals two important results. The first is that the VPI processes have little to no effect on the film microstructure, evidenced by the similar overall "landscape". The second and most important is that the surprising low power conversion efficiency (PCE) reported for this blend[36] is due to a large vertical phase separation that occurs at the 1:1 wt composition. This phase separation was not realized prior to this study due to the lack of experimental techniques that could image the morphology of the BHJ.

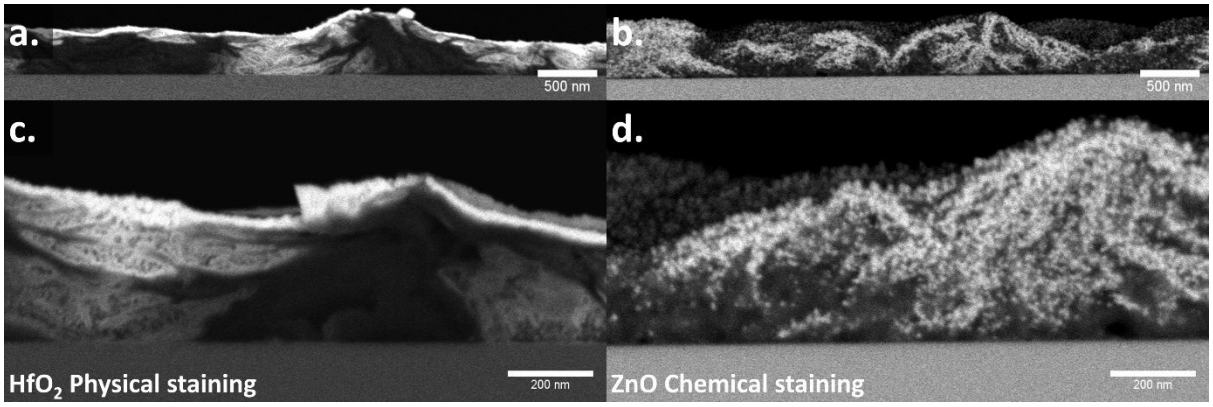

Figure 5- Cross-section HRSEM BSE micrographs of P3HT:ITIC (1:1 wt) blend films after different VPI processes: a. and c.- TDAHf and water; b. and d. DEZ and water. In a. and c., the bright contrast is associated with HfO_2 particles that nucleate and grow in P3HT-rich domains (physical staining) and the dark contrast to impermeable ITIC-rich domains. In b. and d., the bright contrast is associated with ITIC-rich domains due to a chemical reaction between DEZ and ITIC (chemical staining), and the P3HT domains are dark. The selective "staining" in the VPI process effectively maps the phase separation as well as the size- and spatial distribution of the domains in the P3HT:ITIC BHJ. The scale bar for micrographs a. and b. is 500 nm, while for c. and d.it is 200 nm.

To further expand and harness the approach of chemical staining for imaging other NFA molecules, we examined the suitability of this method for the trendy NFA, Y6. Similar to ITIC, Y6 is an ADA NFA but with a dithienothiophen[3.2-b]-pyrrolobenzothiadiazole (TPBT) based donor center unit. The end-capping units are 2-(5,6-Difluoro-3-oxo-2,3-dihydro-1H-inden-1-ylidene)malononitrile (2FIC), similar to those of ITIC, but fluorinated (inset in Figure 6a). To investigate the reactivity of Y6 to DEZ, we measured the UV-vis absorption before and after exposing a Y6 film to the DEZ VPI process. Figure 6a shows that the absorbance features of Y6 (light blue line), i.e., a peak at 812 nm and two shoulders at ~725 and 650 nm[37,38], fade, and a new peak and shoulder rise at 359 and ~330 nm, respectively (purple line). This dramatic color change, from blue to transparent (Figure S9), is similar to that observed for ITIC when exposed to a DEZ VPI process (Figure S1). Therefore, we suggest that Y6 undergo the same

Michael addition during the VPI process involving the nitrile moieties and double bond adjacent to the thiophene ring. This chemical reaction leads to the misty chemical staining, as seen in the cross-section HRSEM micrograph of the Y6 film after the DEZ VPI process (Figure 6b), similar to that of ITIC (Figure 3d).

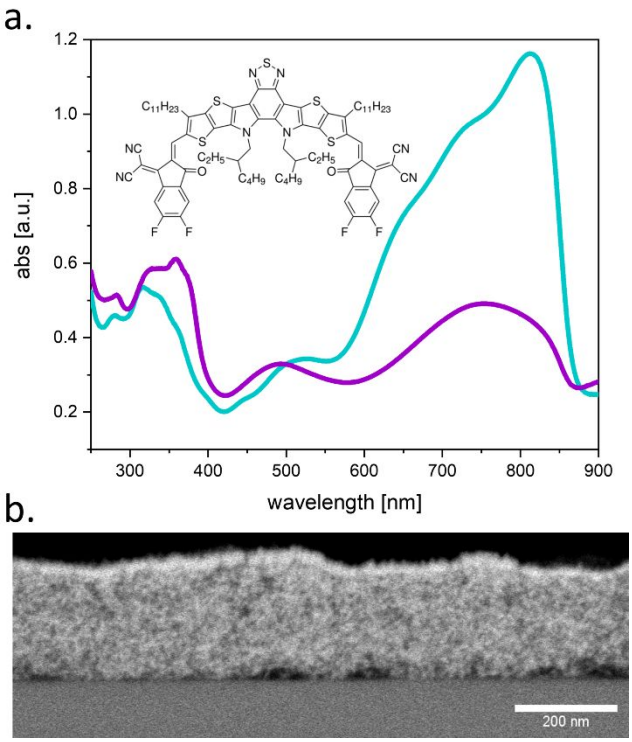

Figure 6- a. UV-vis absorption spectra of a Y6 film before (light blue) and after (purple) exposure to a VPI process of DEZ and water. Inset: chemical structure of Y6. b. Cross-section HRSEM BSE micrograph of a Y6 film after a VPI process of DEZ and water. The micrograph shows fine-textured ZnO "mist" (bright contrast) through the film. The scale bar is 200 nm.

Summary and conclusions

To summarize, we identified a chemical reaction that can be harnessed to chemically stain NFAs with VPI for imaging organic electronic films. We proposed a mechanism for this reaction where the nitrile end-groups of NFAs such as ITIC react with the organometallic DEZ precursor in an addition reaction, effectively reducing the conjugation length. Under such conditions, the abundant nitrile end-groups act as nucleation sites for ZnO, leading to the deposition of very fine ZnO clusters throughout the NFA film. We suggest that this chemical staining process is also suitable for other ADA NFAs that share the same end-capping nitrile moieties and demonstrate this for the commonly used Y6 acceptor. The resulting fine-textured "misty" contrast is distinct from the well-defined nanoparticle character that is

obtained when exposing non-reactive semiconducting polymers, such as P3HT, to the same VPI conditions. Till now, VPI has been used to image the BHJ morphology of fullerene-based devices using this "physical staining" process. We established and compared the BHJ morphology visualization of a polymer:NFA system using both physical and chemical staining and showed that they are complementary, offering new insights into the BHJ morphology. On a broader scope, this work offers a new methodology for imaging the microstructure of complex thin-film organic blends through the judicious selection of reactive/non-reactive precursors to obtain chemical/physical staining for imaging and 3D tomography.

Acknowledgments

We thank Dr. Rachel Edrei from the chemical and surface analysis lab in the Schulich Faculty of Chemistry, Technion, for her help with the chemical analysis. This research was partially supported by the NSF-BSF joint program NSF-funded project #1905901 and BSF #2018652 and the Russell Berrie Nanotechnology Institute in the Technion.

Experimental

Materials, solutions, and films

ITIC and Y6 (purity >99%) were purchased from 1-material. P3HT (40002-EE, Mw 50-70K) was purchased from Rieke metals. DEZ cylinders for use in the ALD system, DEZ (15 wt%) in toluene CB, and chloroform (anhydrous) were purchased from Sigma-Aldrich. The TDAHf ALD precursor cylinder was purchased from Strem Chemicals. All materials were used as received. Poly(3,4-ethylendioxythiophene)–poly(styrenesulfonate) (PEDOT:PSS) for preparing bilayer films was purchased from Solarmer and was filtered in a 0.45 mm PTFE filter before usage.

To study the chemical reaction in solution, two vials with 500 µL of ITIC (20 mg/mL) in CB solution were heated to 60 °C while stirring for 12 hr in an N_2 glove box. 500 µL of DEZ in toluene (15 %wt) were added to one vial, and 500 µL of toluene anhydrous were added to the other and held at 60 °C while stirring for 5 min. The vials were carefully transferred outside of the glove box, and their content was poured into two clean Petri dishes. Both solutions were thermally treated at 115 °C with 100% humidity for 15 min. Solid residues were left in the Petri dishes and used for further analysis.

For film preparation, Si, quartz, and glass substrates were sonicated in acetone, methanol, and isopropanol for 20 min each. Substrates were blow-dried with N_2 gas and transferred to a glovebox with an N_2 atmosphere for film deposition. Two stock solutions of P3HT and ITIC in CB (50 mg/mL, each) were prepared and kept in the glovebox for at least 12 hr@80 °C while stirring. For film deposition, the solutions were diluted to 20 mg/mL. Films were spin-coated onto the selected substrates for 45 sec at 700 rpm followed by 15 sec at 2000 rpm. TA samples were placed on a preheated hot plate for 10 min at 150 °C. All samples were kept in the glove box until introduced to the VPI process. The Si/ITIC/P3HT bilayer samples were prepared by spin coating a PEDOT:PSS solution for 1 min at 3600 rpm onto a glass substrate was, immediately followed by spin coating P3HT; both in an ambient atmosphere. The P3HT film was then floated on DI water and "fished out" on a non-thermally treated ITIC film spun onto a Si substrate. The bilayer samples were not thermally treated.

The BHJ films were spun from a P3HT:ITIC 20:20 mg/mL solution kept for at least 12 hr at 80 °C while stirring. The films were spun onto Si substrates in an N_2 atmosphere glovebox for 45 sec at 700 rpm followed by 15 sec at 2000 rpm. The samples were then thermally annealed for 10 min on a hot plate at 150 °C. All samples were kept in the glove box until used.

Y6 films were spun from a chloroform solution (16 mg/mL) that was kept at RT while stirring for 12 hr. The films were spun onto Si and quartz substrates for 45 sec at 700 rpm followed by 15 sec at 2000 rpm. The films were then thermally annealed for 10 min on a hot plate at 110 °C. All samples were kept in the glove box until used.

Characterization

UV-vis absorption: Thin films on quartz substrates were measured with a Cary 100 scan UV-visible spectrophotometer.

TLC: The solid residues were dissolved in chloroform and placed on a SiO2-coated glass (Thin-layer chromatography (TLC) E. Merck silica gel 60 F254 pre-coated plates (0.25 mm)). As the solvent evaporated, the glass plate was placed in a closed glass tank containing 10 ml of ethyl-acetate:hexane (ratio of 1:9) mixture. The glass was taken out of the solution after 5 min. The different compounds were visible without further chemical staining.

FTIR: The solid residues were grained separately with KBr and compressed to suitable FTIR pallets. FTIR spectroscopy was carried out using a Bruker Tensor 27 in the 4000–400 cm^{-1} range. The scanner velocity was 5 kHz with 4 cm^{-1} resolution. Analysis of the FTIR spectrum was carried out using the OPUS software.

NMR: The solid residues were dissolved in 10 ml DCM (dichloromethane), and 20 ml of water were added to remove zinc salts. The organic layer was separated, and the aqueous layer was extracted three times with 3X10 ml of DCM. The organic fractions were combined and dried over sodium sulfate. The solvent was removed under reduced pressure (rotary evaporation). The product was then dissolved in 0.4ml of $CDCl_3$ and placed in an NMR tube. NMR spectra were recorded on Bruker spectrometers (AVIII400) and are reported relative to deuterated solvent signals. Chemical shifts are reported in parts per million (ppm) with respect to the residual solvent signal CDCl3 (1H NMR: δ = 7.26; 13C NMR: δ = 77.16). Peak multiplicities are reported as follows: s = singlet, bs = broad singlet, d = doublet, t = triplet, dd = doublet of doublets, td = triplet of doublets, m = multiplet.

Mass spectra analysis: High-resolution mass spectra (HRMS) were obtained by the mass spectrometry facility at the Technion.

VPI: All VPI processes were carried out in an Ultratech/Cambridge Nanotech Savannah S200 system.

For the UV-vis measurements, the VPI process was done at 100 °C and 80 consecutive DEZ pulses, followed by a single water pulse. For the ITIC, each DEZ pulse was held for 120 sec, followed by a 15 sec purge. The water pulse was held for 120 sec, followed by a 30 sec purge. For the Y6, each DEZ pulse was held for 900 sec, followed by a 15 sec purge. The water pulse was held for 900 sec, followed by a 30 sec purge. For microscopy characterization, the DEZ and water VPI processes were conducted at 60 or 100 °C (specified) with a carrier gas (N_2) flow rate of 20 or 100 sccm (specified), using 70 alternating cycles of DEZ and water. DEZ was pulsed five consecutive times with 15 sec wait time after each pulse. Then the reaction chamber was purged for 4 min, and water was pulsed once. The reaction chamber was then purged for 5 min, a total of six pulses per cycle. DEZ and water pulse durations were 0.5 and 1 sec, respectively. In the TDAHf and water VPI process, samples were exposed to 40 alternating cycles of TDAHf and water at 100 °C. During each cycle, the samples were exposed

to a TDAHf pulse for 120 sec, followed by a purge process of 30 sec. After the TDAHf pulse, the samples were exposed to an H_2O pulse for 120 sec, followed by a purge process of 40 sec.

HRSEM: micrographs were acquired using a Zeiss Ultra-Plus FEG-SEM operated at 2 kV accelerating voltage with a working distance of 2.4 mm. For cross-section HRSEM imaging, the films on silicon substrates were cleaved in liquid nitrogen.

References

1 Q. Peng, Y. C. Tseng, S. B. Darling and J. W. Elam, *Adv. Mater.*, 2010, **22**, 5129–5133.

2 S. M. Lee, E. Pippel, U. Gösele, C. Dresbach, Y. Qin, C. V. Chandran, T. Bräuniger, G. Hause and M. Knez, *Science (80-.).*, 2009, **324**, 488–492.

3 H. I. Akyildiz, R. P. Padbury, G. N. Parsons and J. S. Jur, *Langmuir*, 2012, **28**, 15697–15704.

4 C. Z. Leng and M. D. Losego, *Mater. Horizons*, 2017, **4**, 747–771.

5 R. Z. Waldman, D. J. Mandia, A. Yanguas-Gil, A. B. F. Martinson, J. W. Elam and S. B. Darling, *J. Chem. Phys.*, 2019, **151**, 190901.

6 S. Obuchovsky, H. Frankenstein, J. Vinokur, A. K. Hailey, Y.-L. Loo and G. L. Frey, *Chem. Mater.*, 2016, **28**, 2668–2676.

7 T. Segal-Peretz, J. Winterstein, M. Doxastakis, A. Ramírez-Hernández, M. Biswas, J. Ren, H. S. Suh, S. B. Darling, J. A. Liddle, J. W. Elam, J. J. de Pablo, N. J. Zaluzec and P. F. Nealey, *ACS Nano*, 2015, **9**, 5333–5347.

8 M. Biswas, J. A. Libera, S. B. Darling and J. W. Elam, *Chem. Mater.*, 2014, **26**, 6135–6141.

9 G. T. Hill, D. T. Lee, P. S. Williams, C. D. Needham, E. C. Dandley, C. J. Oldham and G. N. Parsons, *J. Phys. Chem. C*, 2019, **123**, 16146–16152.

10 M. Biswas, J. A. Libera, S. B. Darling and J. W. Elam, *J. Phys. Chem. C*, 2015, **119**, 14585–14592.

11 E. C. Dandley, C. D. Needham, P. S. Williams, A. H. Brozena, C. J. Oldham and G. N. Parsons, *J. Mater. Chem. C*, 2014, **2**, 9416–9424.

12 I. Weisbord, N. Shomrat, R. Azoulay, A. Kaushansky and T. Segal-Peretz, *Chem. Mater.*, 2020, **32**, 4499–4508.

13 M. Biswas, J. A. Libera, S. B. Darling and J. W. Elam, *Chem. Mater.*, 2014, **26**, 6135–6141.

14 R. P. Padbury and J. S. Jur, *Langmuir*, 2014, **30**, 9228–9238.

15 J. S. Jur, J. C. Spagnola, K. Lee, B. Gong, Q. Peng and G. N. Parsons, *Langmuir*, 2010, **26**, 8239–8244.

16 Y. C. Tseng, Q. Peng, L. E. Ocola, D. A. Czaplewski, J. W. Elam and S. B. Darling, *J. Mater. Chem.*, 2011, **21**, 11722–11725.

17 I. Azpitarte and M. Knez, *MRS Commun.*, 2018, **8**, 727–741.

18 B. K. Barick, A. Simon, I. Weisbord, N. Shomrat and T. Segal-Peretz, *J. Colloid Interface Sci.*, 2019, **557**, 537–545.

19 S. Obuchovsky, B. Shamieh, I. Deckman, G. Ankonina and G. L. Frey, *Sol. Energy Mater. Sol. Cells*, 2015, **143**, 280–283.

20 M. Moshonov and G. L. Frey, *Langmuir*, 2015, **31**, 12762–12769.

21 S. Obuchovsky, M. Levin, A. Levitsky and G. L. Frey, *Org. Electron.*, 2017, **49**, 234–241.

22 L. Zhang, F. Li, Y. Chen, X. Peng and W. Zhou, *J. Lumin.*, 2010, **130**, 2332–2338.

23 A. Mahmood and J.-L. Wang, *Sol. RRL*, 2020, **4**, 2000337.

24 D. Chen, A. Nakahara, D. Wei, D. Nordlund and T. P. Russell, *Nano Lett.*, 2011, **11**, 561–567.

25 A. Levitsky, G. Maria Matrone, A. Khirbat, I. Bargigia, X. Chu, O. Nahor, T. Segal-Peretz, A. J. Moulé, L. J. Richter, C. Silva, N. Stingelin and G. L. Frey, *Adv. Sci.*, 2020, **7**, 2000960.

26 A. Levitsky, S. A. Schneider, E. Rabkin, M. F. Toney and G. L. Frey, *Mater. Horizons*, 2021, **8**, 1272–1285.

27 Y. Lin, J. Wang, Z.-G. Zhang, H. Bai, Y. Li, D. Zhu and X. Zhan, *Adv. Mater.*, 2015, **27**, 1170–1174.

28 A. Armin, W. Li, O. J. Sandberg, Z. Xiao, L. Ding, J. Nelson, D. Neher, K. Vandewal, S. Shoaee, T. Wang, H. Ade, T. Heumüller, C. Brabec and P. Meredith, *Adv. Energy Mater.*, 2021, 11, 2003570.

29 J. Hou, O. Inganäs, R. H. Friend and F. Gao, *Nat. Mater.*, 2018, **17**, 119.

30 H. Liu, W. Wang, Y. Zhou and Z. Li, *J. Mater. Chem. A*, 2021, **9**, 1080–1088.

31 O. Nahor, T. Segal-Peretz, L. Neeman, D. Oron and G. L. Frey, *J. Mater. Chem. C*, 2014, **2**, 4167–4176.

32 R. M. Silverstein, *Spectrometric identification of organic compounds*, Wiley, Hoboken, NJ, Eighth edi., 2015.

33 M. P. Bernstein, S. A. Sandford and L. J. Allamandola, *Astrophys. J.*, 1997, **476**, 932–942.

34 S. Park and H. J. Son, *J. Mater. Chem. A*, 2019, **7**, 25830–25837.

35 S. Obuchovsky, I. Deckman, M. Moshonov, T. Segal Peretz, G. Ankonina, T. J. Savenije and G. L. Frey, *J. Mater. Chem. C*, 2014, **2**, 8903–8910.

36 Y. Qin, M. A. Uddin, Y. Chen, B. Jang, K. Zhao, Z. Zheng, R. Yu, T. J. Shin, H. Y. Woo and J. Hou, *Adv. Mater.*, 2016, **28**, 9416–9422.

37 X. Zou, G. Wen, R. Hu, G. Dong, C. Zhang, W. Zhang, H. Huang and W. Dang, *Molecules*, 2020, 25.

38 J. Yuan, Y. Zhang, L. Zhou, G. Zhang, H.-L. Yip, T.-K. Lau, X. Lu, C. Zhu, H. Peng, P. A. Johnson, M. Leclerc, Y. Cao, J. Ulanski, Y. Li and Y. Zou, *Joule*, 2019, **3**, 1140–1151.